Desalination and Water Treatment
www.deswater.com

doi: 10.1080/19443994.2014.937750

55 (2015) 2009–2022
August

Taylor & Francis
Taylor & Francis Group

Two-phase flow numerical simulation and experimental verification of falling film evaporation on a horizontal tube bundle

S. Bigham[a], R. KouhiKamali[b,*], S.M.A. Noori Rahim Abadi[b]

[a]*School of Mechanical Engineering, University of Tehran, Tehran, Iran, Tel. +13528710402; email: sajjadbigham@gmail.com*
[b]*Department of Mechanical Engineering, University of Guilan, Rasht, Iran, Tel. +98 131 6690276; email: kouhikamali@guilan.ac.ir (R. KouhiKamali), Tel. +98 21 44144877; email: a.noori1364@gmail.com (S.M.A. Noori Rahim Abadi)*

Received 7 September 2013; Accepted 27 May 2014

ABSTRACT

In this study, a two-phase flow investigation on falling film evaporation phenomenon is described. To track liquid–vapor interface, the volume of fluid multiphase model based on the piecewise linear interface construction method in curvilinear coordinate is used. A finite volume method code based on the SIMPLE algorithm and non-orthogonal discretization grid system is used for solving the governing equations including continuity, energy, and Reynolds averaged Navier–Stokes equations with the k–ε turbulence model. Also, the energy and mass transfer during the phase change is taken into account. The effects of inlet mass flow rate and temperature difference between the tube temperature and the saturation temperature on the local and average heat transfer coefficient and the net vapor production are presented. Results show the average heat transfer coefficient increases/decreases by increasing in the inlet mass flow rate/the temperature difference at a constant temperature difference/inlet mass flow rate. Results also demonstrate at a constant value of $\Delta T/\dot{m}_f$ (MED-TVC design approach), as the inlet mass flow rate increases, the heat transfer coefficient may be decreased or increased. This increase or decrease depends on the values of $\Delta T/\dot{m}_f$ and ΔT.

Keywords: Falling film evaporation; VOF method; Curvilinear coordinate; Two phase flow; MED-TVC units

1. Introduction

Two-phase flow on a bundle tube along with evaporation phenomenon is an important problem that takes place in industrial devices such as heat exchangers and sea water desalination units. Falling film evaporation is also used in the petrochemical industry as well as large heat pump systems.

One of the prominent factors in the design of thermal industrial devices is the heat transfer coefficient on the evaporating side of the tubes. In spite of the fact that there are some empirical correlations for determining the overall heat transfer coefficient of a bundle tube, these correlations are presented for their particular geometry and flow condition. So, the numerical simulation of such complicated flows that encounter the evaporation process can be extremely helpful in an accurate thermal design.

In falling film evaporation systems, the fluid that flows downward by gravity will create a film along the tube walls. As the film flows around the tubes, it becomes warmer. The falling liquid film starts

---

*Corresponding author.

evaporating when the temperature of the falling liquid reaches the saturation temperature. The heat transfer coefficient may be affected by several parameters. As the process proceeds, the portion of vapor increases. Because the density of vapor is lower than the density of liquid, the conservation of mass dictates that the vapor velocity should be increased. By increasing the velocity of vapor, the shear stress between the liquid and vapor and the liquid velocity are increased resulting in intensifying turbulent flow. As a result, the heat transfer coefficient is increased in falling film evaporation. In addition, nucleate boiling often occurring in falling film evaporation systems augments the value of heat transfer coefficient. On the contrary, by increasing the heat flux, dry patches may occur on the surface of the tubes which results in decreasing the heat transfer coefficient.

Falling film evaporation phenomenon has been widely studied by numerous researchers [1–4]. A state-of-the-art review of falling film evaporation on single tubes and tube bundles is presented by Thome [5]. Both plain and enhanced tubes are addressed in his survey plus the effects of oil on heat transfer. He concluded that the enhanced tubes provide a very high level of heat transfer augmentation for falling film evaporation on horizontal bundles, sharply reducing the required refrigerant charge compared to flooded evaporator designs. Chyu and Bergles [6] developed an analytical model for predicting the heat transfer coefficient of falling film evaporation on a horizontal tube. Their solution considered four separate zones around the circumference of the tube: stagnation flow, impingement, thermal developing/developed with heating of the liquid, and fully developed region with surface evaporation. Their results showed that for the case of saturated falling films, convective heat transfer leads to evaporation at the liquid–vapor interface. By increasing heat flux, nucleate boiling occurs; vapor bubbles grow and are carried along by the film flow such that both the thin falling film evaporation and nucleate boiling play a role in the heat transfer process, depending mainly on the heat flux and liquid mass flow. Falling thin-film heat transfer on horizontal smooth tubes had been examined by Parken et al. [7]. They found that the average boiling heat transfer coefficients increase by increasing the feedwater temperature and tube-wall heat flux, and increase slightly by increasing flow rate. Yang and Shen [8] carried out an experimental study of falling film heat transfer outside horizontal tubes in order to show how the heat transfer coefficient is affected by different parameters. Their results showed that the heat transfer coefficient of falling film evaporation outside horizontal tubes increases by the increase in the liquid feeding, evaporation boiling temperature, and heat flux. Habert and Thome [9,10] performed falling film evaporation measurements on a single tube row bundle and a three-row tube bundle to obtain local heat transfer coefficients. They observed that in a single-row configuration, the heat transfer coefficient is mostly constant for a given heat flux in the plateau region until the onset of dryout is reached, followed by increasing dryout of the surface with a rapid decrease of the heat transfer toward the vapor phase heat transfer value at complete dryout. They also concluded that the bundle effects were detrimental to thermal performance. They discussed that the hydrodynamics of the liquid film appeared to be the key parameter and flow is actually a bubbly two-phase flow, not a liquid film.

In this work, boundary conditions have curvy walls. Considerable efforts have been devoted to simulate fluid flow and heat transfer in curved geometries [11,12]. In these problems, a transformation from physical space to computational space is introduced. This transformation is accomplished by specifying a generalized coordinate system, which will map the non-rectangular grid system, and change the physical space to a rectangular uniform grid spacing in the computational space.

With the recent advent of high-speed computers, the numerical techniques for the simulation of two-phase flow with liquid–vapor phase change have become very promising. Yang et al. [13] performed volume of fluid (VOF) simulations of boiling flow of R141B in a horizontal coiled tube. The calculations treated the phase change as a local temperature dictated process based on a quasi thermo-equilibrium assumption, which yielded a flow pattern in good agreement with the experimental observation. Son and Dhir [14] used a coordinate transformation technique, supplemented by a numerical grid generation method, to simulate film boiling for both two-dimensional and axisymmetric flows. Yuan et al. [15] presented a numerical method for the simulation of boiling flows on non-orthogonal body-fitted coordinates via VOF method based on piecewise linear interface construction (PLIC) for tracking liquid–vapor interface. They simulated natural convection film boiling and forced convection film boiling on a sphere at saturated conditions.

The main purpose of this work is to investigate how the local and average heat transfer coefficient can be affected by the inlet mass flow rate and the temperature difference in falling film evaporation systems. Also, another aspect of this work is to find out in which condition the effect of the inlet mass flow rate or the temperature difference on heat transfer coefficient is dominant when both of them are changed.

2. Mathematical formulation

The tube bundles layout is shown schematically in Fig. 1. In the falling film process, water is distributed on the top of tube bundles. As water flows around the hot tubes, heat conveys from the tube to the fluid. During this process, the temperature of the liquid increases and some parts of liquid may be evaporated. So, there are two phases, e.g. the liquid phase as well as the vapor phase. The volume fraction of each phase is obtained by solving the continuity equation for the phase volume fraction. In each computational cell, the volume fractions of two phases sum to unity. This means that the volume fraction equation does not need to be solved for one of the phases and can be computed based on the following constraint:

$$\alpha_l = 1 - \alpha_v \tag{1}$$

Information on phase distribution and the tracking of the interfaces between the different phases throughout the solution domain are accomplished by the solution of continuity equations for the volume fraction of different phases. In order to solve the continuity equations, the velocity field should be known. The VOF method assumes that all phases have a common velocity field that is obtained from Reynolds-averaged Navier–Stokes equations (RANS equations). Once the velocity field is determined, the continuity equation can be solved. For the vapor phase, this equation has the following form:

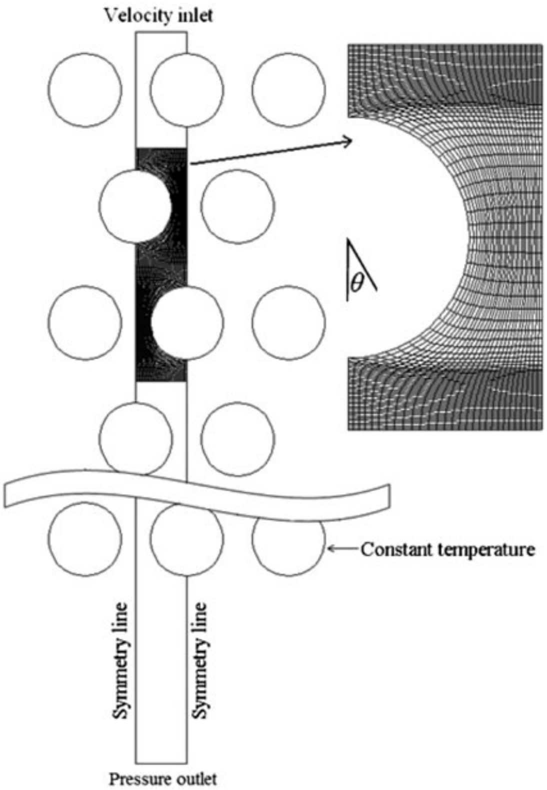

Fig. 1. The physical domain of the tube bundle.

$$\frac{\partial}{\partial x}(\rho_v \alpha_v u) + \frac{\partial}{\partial y}(\rho_v \alpha_v v) = S_v \tag{2}$$

Because of the special geometry of the present problem, a general non-orthogonal curvilinear coordinate framework with (ξ, η) as independent variables is used to formulate the problem. In curvilinear coordinate, the continuity equation has the following form:

$$\frac{\partial}{\partial \xi}\left(\rho_v \alpha_v U^C\right) + \frac{\partial}{\partial \eta}\left(\rho_v \alpha_v V^C\right) = J S_v \tag{3}$$

where

$$\begin{aligned} &U^C = \left(u y_\eta - v x_\eta\right), \quad V^C = \left(-u y_\xi + v x_\xi\right), \\ &J = \left(x_\xi y_\eta - x_\eta y_\xi\right) \end{aligned} \tag{4}$$

Using the above equation, the volume fraction of each phase is determined. The fields for all variables and properties are shared by the phases and represent volume-averaged values, as long as the volume fraction of each of the phases is known at each location. It should be noted, however, the phase-volume fraction values do not uniquely identify the interface between the phases. Several specialized techniques are developed to track the interfacial geometry accurately [16]. The VOF method assumes that the interface is a continuous, piecewise smooth line in each computational cell. In fact, these piecewise linear segments construct the interface. The slope of interface line is determined from the interface norm. These lines divide the computational cell into sections in such a way that the volume of the phases in the cell corresponds with the values of the phase volume fractions in that cell. The problem of finding these piecewise smooth lines is really challenging and several techniques are developed. These techniques are generally known as the Piecewise Linear Interface Calculation algorithms [17].

As mentioned before, in VOF method, there is a unique velocity field shared by all phases. This velocity field is obtained by solving a single momentum equation throughout the domain. Falling film evaporation is inherently turbulent. So, the RANS equations, which are time-averaged equations of motion for fluid flow, are used. The idea behind the equations is Reynolds decomposition, whereby an instantaneous quantity is decomposed into its time-averaged and fluctuating quantities. RANS equations are as following:

RANS equation in ξ-direction:

$$\begin{aligned}\frac{\partial}{\partial\xi}\left(\rho u U^{C}\right)+\frac{\partial}{\partial\eta}\left(\rho u V^{C}\right)=&\left\{\frac{\partial}{\partial\xi}\left(q_{11}\mu\frac{\partial u}{\partial\xi}\right)\right.\\&+\frac{\partial}{\partial\xi}\left(q_{12}\mu\frac{\partial u}{\partial\eta}\right)+\frac{\partial}{\partial\eta}\left(q_{12}\mu\frac{\partial u}{\partial\xi}\right)+\left.\frac{\partial}{\partial\eta}\left(q_{22}\mu\frac{\partial u}{\partial\eta}\right)\right\}\\&-\left\{\frac{\partial}{\partial\xi}\left(y_\eta p\right)-\frac{\partial}{\partial\eta}\left(y_\xi p\right)\right\}+JS_{uvd}+JS_{uturb}\end{aligned}\tag{5}$$

where

$$\begin{aligned}JS_{\mathrm{uvd}}=&\frac{1}{3}\frac{\partial}{\partial\xi}\left[\frac{1}{J}\left({y_\eta}^2\mu\frac{\partial u}{\partial\xi}-y_\xi y_\eta\mu\frac{\partial u}{\partial\eta}-x_\eta y_\eta\mu\frac{\partial v}{\partial\xi}+x_\xi y_\eta\mu\frac{\partial v}{\partial\eta}\right)\right]\\&+\frac{1}{3}\frac{\partial}{\partial\eta}\left[\frac{1}{J}\left(-y_\xi y_\eta\mu\frac{\partial u}{\partial\xi}+{y_\xi}^2\mu\frac{\partial u}{\partial\eta}+x_\eta y_\xi\mu\frac{\partial v}{\partial\xi}-x_\xi y_\xi\mu\frac{\partial v}{\partial\eta}\right)\right]\end{aligned}\tag{6}$$

$$\begin{aligned}JS_{\mathrm{uturb}}=&\sum_{j=1}^{2}\frac{\partial}{\partial x_j}\left(-\rho\overline{u'u'_j}\right)\\=&\left\{\frac{\partial}{\partial\xi}\left(q_{11}\mu_t\frac{\partial u}{\partial\xi}\right)+\frac{\partial}{\partial\xi}\left(q_{12}\mu_t\frac{\partial u}{\partial\eta}\right)+\frac{\partial}{\partial\eta}\left(q_{12}\mu_t\frac{\partial u}{\partial\xi}\right)+\frac{\partial}{\partial\eta}\left(q_{22}\mu_t\frac{\partial u}{\partial\eta}\right)\right\}\\&+\frac{1}{3}\frac{\partial}{\partial\xi}\left[\frac{1}{J}\left({y_\eta}^2\mu_t\frac{\partial u}{\partial\xi}-y_\xi y_\eta\mu_t\frac{\partial u}{\partial\eta}-x_\eta y_\eta\mu_t\frac{\partial v}{\partial\xi}+x_\xi y_\eta\mu_t\frac{\partial v}{\partial\eta}\right)\right]\\&+\frac{1}{3}\frac{\partial}{\partial\eta}\left[\frac{1}{J}\left(-y_\xi y_\eta\mu_t\frac{\partial u}{\partial\xi}+{y_\xi}^2\mu_t\frac{\partial u}{\partial\eta}+x_\eta y_\xi\mu_t\frac{\partial v}{\partial\xi}-x_\xi y_\xi\mu_t\frac{\partial v}{\partial\eta}\right)\right]\\&-\frac{2}{3}\rho\left\{\frac{\partial}{\partial\xi}\left(y_\eta k\right)-\frac{\partial}{\partial\eta}\left(y_\xi k\right)\right\}\end{aligned}\tag{7}$$

$$q_{11}=\left(\frac{{x_\eta}^2+{y_\eta}^2}{J}\right),\quad q_{22}=\left(\frac{{x_\xi}^2+{y_\xi}^2}{J}\right),\quad q_{12}=\left(-\frac{x_\xi x_\eta+y_\xi y_\eta}{J}\right)\tag{8}$$

where q_{11}, q_{12}, and q_{22} are metric tensors which allow us to compute the distances in any coordinate system. As it is clear from the Eq. (8), tensor q is a symmetric tensor. In this way, the notion of metric associated to a space, emerges in a natural way.

RANS equation in η-direction:

$$\begin{aligned}\frac{\partial}{\partial\xi}\left(\rho v U^{C}\right)+\frac{\partial}{\partial\eta}\left(\rho v V^{C}\right)=&\left\{\frac{\partial}{\partial\xi}\left(q_{11}\mu\frac{\partial v}{\partial\xi}\right)+\frac{\partial}{\partial\xi}\left(q_{12}\mu\frac{\partial v}{\partial\eta}\right)+\frac{\partial}{\partial\eta}\left(q_{12}\mu\frac{\partial v}{\partial\xi}\right)+\frac{\partial}{\partial\eta}\left(q_{22}\mu\frac{\partial v}{\partial\eta}\right)\right\}\\&-\left\{-\frac{\partial}{\partial\xi}\left(x_\eta p\right)+\frac{\partial}{\partial\eta}\left(x_\xi p\right)\right\}-\rho g+JS_{vvd}+JS_{vturb}\end{aligned}\tag{9}$$

where

$$\begin{aligned}JS_{vvd}=&\frac{1}{3}\frac{\partial}{\partial\xi}\left[\frac{1}{J}\left(-x_\eta y_\eta\mu\frac{\partial u}{\partial\xi}+x_\eta y_\xi\mu\frac{\partial u}{\partial\eta}+{x_\eta}^2\mu\frac{\partial v}{\partial\xi}-x_\xi x_\eta\mu\frac{\partial v}{\partial\eta}\right)\right]\\&+\frac{1}{3}\frac{\partial}{\partial\eta}\left[\frac{1}{J}\left(-x_\xi y_\eta\mu\frac{\partial u}{\partial\xi}-x_\xi y_\xi\mu\frac{\partial u}{\partial\eta}-x_\xi x_\eta\mu\frac{\partial v}{\partial\xi}+{x_\xi}^2\mu\frac{\partial v}{\partial\eta}\right)\right]\end{aligned}\tag{10}$$

$$\begin{aligned}JS_{uturb}=&\sum_{j=1}^{2}\frac{\partial}{\partial x_j}\left(-\rho\overline{v'u'_j}\right)\\=&\left\{\frac{\partial}{\partial\xi}\left(q_{11}\mu_t\frac{\partial v}{\partial\xi}\right)+\frac{\partial}{\partial\xi}\left(q_{12}\mu_t\frac{\partial v}{\partial\eta}\right)+\frac{\partial}{\partial\eta}\left(q_{12}\mu_t\frac{\partial v}{\partial\xi}\right)+\frac{\partial}{\partial\eta}\left(q_{22}\mu_t\frac{\partial v}{\partial\eta}\right)\right\}\\&+\frac{\mu_t}{3}\left(JS_{vvd}\right)-\frac{2}{3}\rho\left\{-\frac{\partial}{\partial\xi}\left(x_\eta k\right)+\frac{\partial}{\partial\eta}\left(x_\xi k\right)\right\}\end{aligned}\tag{11}$$

The turbulent kinetic energy k and its dissipation rate ε obey their own transport equation as:

$$\begin{aligned}\frac{\partial}{\partial\xi}\left(\rho k U^{C}\right)+\frac{\partial}{\partial\eta}\left(\rho k V^{C}\right)=&\left\{\frac{\partial}{\partial\xi}\left(q_{11}(\mu+\mu_t)\frac{\partial k}{\partial\xi}\right)\right.\\&+\frac{\partial}{\partial\xi}\left(q_{12}(\mu+\mu_t)\frac{\partial k}{\partial\eta}\right)+\frac{\partial}{\partial\eta}\left(q_{12}(\mu+\mu_t)\frac{\partial k}{\partial\xi}\right)\\&+\left.\frac{\partial}{\partial\eta}\left(q_{22}(\mu+\mu_t)\frac{\partial k}{\partial\eta}\right)\right\}-\rho\varepsilon+JG_k\end{aligned}\tag{12}$$

$$\begin{aligned}\frac{\partial}{\partial\xi}\left(\rho\varepsilon U^{C}\right)+\frac{\partial}{\partial\eta}\left(\rho\varepsilon V^{C}\right)=&\left\{\frac{\partial}{\partial\xi}\left(q_{11}(\mu+0.77\mu_t)\frac{\partial\varepsilon}{\partial\xi}\right)\right.\\&+\frac{\partial}{\partial\xi}\left(q_{12}(\mu+0.77\mu_t)\frac{\partial\varepsilon}{\partial\eta}\right)+\frac{\partial}{\partial\eta}\left(q_{12}(\mu+0.77\mu_t)\frac{\partial\varepsilon}{\partial\xi}\right)\\&+\left.\frac{\partial}{\partial\eta}\left(q_{22}(\mu+0.77\mu_t)\frac{\partial\varepsilon}{\partial\eta}\right)\right\}-1.92\rho\frac{\varepsilon^2}{k}+\frac{1.44\varepsilon}{k}JG_k\end{aligned}\tag{13}$$

where

$$\mu_t=0.09\,\rho\frac{k^2}{\varepsilon}\tag{14}$$

$$\begin{aligned}G_k=&\frac{4}{3}\left(\frac{u_\xi y_\eta-u_\eta y_\xi}{J}\right)^2+\frac{4}{3}\left(\frac{-v_\xi x_\eta+v_\eta x_\xi}{J}\right)^2\\&-\frac{4}{3}\left(\frac{u_\xi y_\eta-u_\eta y_\xi}{J}\right)\left(\frac{-v_\xi x_\eta+v_\eta x_\xi}{J}\right)\\&+2\left(\frac{-u_\xi x_\eta+u_\eta x_\xi}{J}\right)\left(\frac{v_\xi y_\eta-v_\eta y_\xi}{J}\right)\\&+\left(\frac{-u_\xi x_\eta+u_\eta x_\xi}{J}\right)^2+\left(\frac{v_\xi y_\eta-v_\eta y_\xi}{J}\right)^2\\&-\frac{2}{3}\rho k\left(\frac{u_\xi y_\eta-u_\eta y_\xi-v_\xi x_\eta+v_\eta x_\xi}{J}\right)\end{aligned}\tag{15}$$

The velocity field is subject to the incompressibility constraint:

$$\frac{\partial}{\partial \xi}\left(U^{C}\right)+\frac{\partial}{\partial \eta}\left(V^{C}\right)=0 \tag{16}$$

It is worthwhile to mention that the above equation is used for obtaining the pressure correction equation in SIMPLE algorithm and VOF model. In fact, to obtain the pressure correction equation, the liquid and vapor phases are treated as one phase. Notice that Eqs. (1) and (3) are used to obtain the vapor and liquid volume fractions.

In order to avoid abrupt changes across very thin interfaces, a volume-weighted interpolation scheme is used for mixture properties in the RANS equations as below:

$$\rho=\alpha_{l}\rho_{l}+\alpha_{v}\rho_{v} \tag{17}$$

$$\mu=\alpha_{l}\mu_{l}+\alpha_{v}\mu_{v} \tag{18}$$

In the VOF model, a unique energy equation is solved throughout the computational domain and the obtained temperature is shared by all phases.

$$\begin{aligned}\frac{\partial}{\partial \xi}\left(\rho\chi U^{C}T\right)+\frac{\partial}{\partial \eta}\left(\rho\chi V^{C}T\right)=&\frac{\partial}{\partial \xi}\left(q_{11}\frac{\partial}{\partial \xi}(KT)\right)\\&+\frac{\partial}{\partial \xi}\left(q_{12}\frac{\partial}{\partial \eta}(KT)\right)\\&+\frac{\partial}{\partial \eta}\left(q_{12}\frac{\partial}{\partial \xi}(KT)\right)\\&+\frac{\partial}{\partial \eta}\left(q_{22}\frac{\partial}{\partial \eta}(KT)\right)+JS_{E}\end{aligned} \tag{19}$$

where the thermal conductivity is calculated as:

$$K=\alpha_{l}K_{l}+\alpha_{v}K_{v} \tag{20}$$

In the VOF model, the total energy is treated as mass-averaged variables as the following:

$$E=\frac{\alpha_{v}\rho_{v}E_{v}+\alpha_{l}\rho_{l}E_{l}}{\alpha_{v}\rho_{v}+\alpha_{l}\rho_{l}} \tag{21}$$

If the total energy is treated as above, χ has the following form:

$$\chi=\frac{\alpha_{l}\rho_{l}C_{v,l}+\alpha_{v}\rho_{v}C_{v,v}}{\alpha_{l}\rho_{l}+\alpha_{v}\rho_{v}} \tag{22}$$

As long as the energy equation is solved, the temperature distribution is obtained throughout the computational domain. At this point, it is useful to recall two physical facts:

(1) If the liquid temperature becomes greater than the saturated temperature at a given pressure, the liquid will evaporate.
(2) If the vapor temperature becomes less than the saturated temperature at a given pressure, the condensation will occur.

It means that, in a computational cell, the evaporation or condensation will take place based on the cell temperature and the mass of the phases. When the evaporation occurs, mass is transferred from liquid phase to the vapor phase, i.e. the mass of liquid phase decreases and the mass of vapor phase increases correspondingly. The magnitude of the evaporation process is calculated by Lee [18] as:

$$S_{v}=\beta_{1}\alpha_{l}\rho_{l}\left|\frac{T-T_{\text{sat}}}{T_{\text{sat}}}\right| \tag{23}$$

Similarly for the condensation process:

$$S_{l}=\beta_{2}\alpha_{v}\rho_{v}\left|\frac{T-T_{\text{sat}}}{T_{\text{sat}}}\right| \tag{24}$$

where β_1 and β_2 are the mass transfer time relaxation parameters which are defined as:

$$\beta_{1}=\frac{6}{D_{\text{Sm}}}\frac{\sqrt{M}}{\sqrt{2\pi RT_{\text{sat}}}}\frac{\rho_{v}h_{lv}}{\rho_{l}-\rho_{v}} \tag{25}$$

$$\beta_{2}=\frac{6}{D_{\text{Sm}}}\frac{\sqrt{M}}{\sqrt{2\pi RT_{\text{sat}}}}\frac{\rho_{l}h_{lv}}{\rho_{l}-\rho_{v}} \tag{26}$$

where D_{Sm} and $h_{\text{l}v}$ are mean Sauter diameter and latent heat, respectively [19]. In order to numerically maintain the interfacial temperature within $T_{\text{sat}} \pm 1$ K, β_1 and β_2 need to be finely tuned. Large values of these parameters induce a numerical oscillation, whereas too small values cause the interfacial temperature to substantially deviate from T_{sat} [13].

It should be noticed that the evaporation or condensation process includes not only mass transfer but also heat transfer. In the evaporation process, the liquid phase is converted into the vapor phase. This process causes the liquid temperature not to increase in value above the saturation temperature. So, in numerical simulation, a negative source should be added to the energy equation. Correspondingly, there is a similar phenomenon in the condensation process. The heat transfer corresponding with the evaporation or condensation process is determined by multiplying the calculated mass transfer with the latent heat, i.e. for the evaporation process:

$$S_E = -S_v h_{lv} \tag{27}$$

and for the condensation process:

$$S_E = S_l h_{lv} \tag{28}$$

The fluid velocity and water mass-flow rate in y-direction (or η-direction) is defined at the inlet boundary condition. In addition, at the inlet, the fluid velocity in x-direction (ξ-direction) and the fluid temperature are equal to zero and the saturation temperature, respectively. So,

$$u = 0,\ v = v_{\text{in}},\ T = T_{\text{sat}} \tag{29}$$

At the outlet, it is assumed that the fluid has reached a terminal velocity. Furthermore, the fluid temperature is equal to the saturation temperature. It is worthwhile to mention that in this study, change in saturation temperature due to the pressure drop is not taken into account. Therefore

$$u = 0,\ \frac{\partial v}{\partial y} = 0,\ T = T_{\text{sat}} \tag{30}$$

The boundary conditions at the tube wall are:

$$u = 0,\ \text{v} = 0,\ T = T_w \tag{31}$$

and symmetry condition is assumed at the right and the left of the computational domain as follows:

$$u = 0,\ \frac{\partial \text{v}}{\partial y} = 0,\ \frac{\partial T}{\partial y} = 0 \tag{32}$$

The heat transfer coefficient at the tube wall is calculated by

$$h = \frac{-k_l \frac{\partial T}{\partial n}}{T_w - T_{\text{sat}}} = \frac{-k_l}{T_w - T_{\text{sat}}} \frac{1}{\sqrt{J q_{22}}} \left(q_{11} \frac{\partial T}{\partial \xi} + q_{22} \frac{\partial T}{\partial \eta} \right) \tag{33}$$

3. Validation of numerical code

In Fig. 2, a comparison with the previously published result of Parken et al. [7] is done to validate the numerical code and non-orthogonal grid discretization scheme of the present study. Their experimental setup is analogous to the present model. As observed, the numerical results are in good agreement with available experimental data.

4. Grid dependence

The accuracy of the numerical solutions and the time required to reach a steady-state solution are dependent on the grid resolution. To clarify the effect of mesh refinement on the numerical solution, three meshes are used in the numerical analysis: 500 × 40, 450 × 35, and 400 × 30. As shown in Fig. 3, increasing the grid numbers does not significantly change in the local heat transfer coefficient. For the $\Delta T = 4.75$°C and $\dot{m} = 0.005\,\text{kg/s}$, 450 × 35 grid seems to be optimum in accuracy and run time. Furthermore, a similar type of grid independence study is carried out for the other Knudsen and Re numbers (not reported here) and optimum meshes are chosen.

5. Solution procedure

The governing equations with appropriate boundary conditions are solved by employing the SIMPLE algorithm [20], a finite-volume method, in a non-orthogonal curvilinear coordinate framework. The Poisson equations are solved for (x, y) to find grid

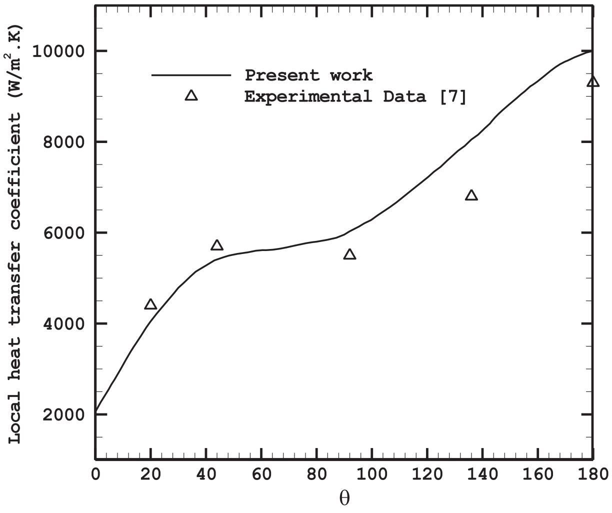

Fig. 2. Validation of numerical code with available data.

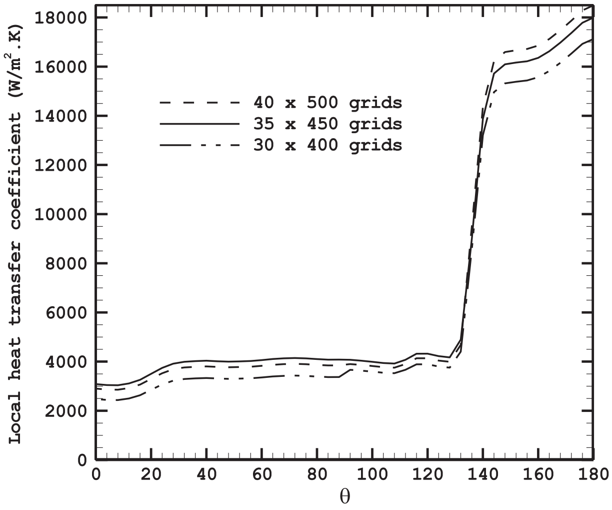

Fig. 3. Numerical results of local heat transfer coefficient around the tube wall at $\Delta T = 4.75$°C and $\dot{m} = 0.005\,\mathrm{kg/s}$.

points [21] and are distributed in a non-uniform manner with higher concentration of grids close to the curvy walls and normal to all walls, as shown in Fig. 1. In this work, a fully implicit scheme is used for the temporal terms and the HYBRID differencing [22] is applied for the approximation of the convective terms in a full-staggered grid. In addition, the tridiagonal matrix algorithm scheme is used to solve the discrete algebraic equations. The governing equations are solved by a successive over relaxation method and for convergence, an under-relaxation technique is employed.

One convergence criterion is a mass flux residual less than 10^{-7} for each control volume. Another criterion is $(|\varphi^{i+1} - \varphi^{i}|)/|\varphi^{i+1}| \leq 10^{-8}$ where φ represents any dependent variable, namely u, v, and T, and i is the number of iterations.

6. Results and discussion

To have a physical point of view, and for the purpose of calculating the fluid flow and heat transfer characteristics, numerical calculations are carried out for different values of the inlet mass flow rates and the temperature differences. Because of the symmetrical geometry, in this work, only one part of the original geometry shown in Fig. 1 is numerically solved. Therefore, the time of computation work is reduced considerably. The following results are obtained for the typical values of parameters as: $T_{\mathrm{sat}} = 321.65\,\mathrm{K}$, $\rho_{\mathrm{l}} = 988.7\,\mathrm{kg/m^3}$, $\rho_v = 0.077\,\mathrm{kg/m^3}$, $C_{v,\mathrm{l}} = 4{,}327\,\mathrm{J/kg\,K}$, $C_{v,v} = 1{,}465\,\mathrm{J/kg\,K}$, $\mu_{\mathrm{l}} = 560\,\mu\mathrm{Ps\,s}$, and $\mu_v = 10.57\,\mu\mathrm{Pa\,s}$.

Fig. 4 shows the fluid velocity vector around the tube at $\Delta T = 9.5$°C and $\dot{m}_f = 0.001\,\mathrm{kg/s}$. As can be seen, at the upper side of the tube, the direction of the fluid is downstream. This direction demonstrates that the majority of the fluid in this region is liquid water. This liquid water flows downstream with gravitational force. On the other hand, at the lower side of the tube, the fluid direction around the tube is upstream. This direction illustrates the fact that the major portion of the fluid in this region is water vapor and is inclined to move upward.

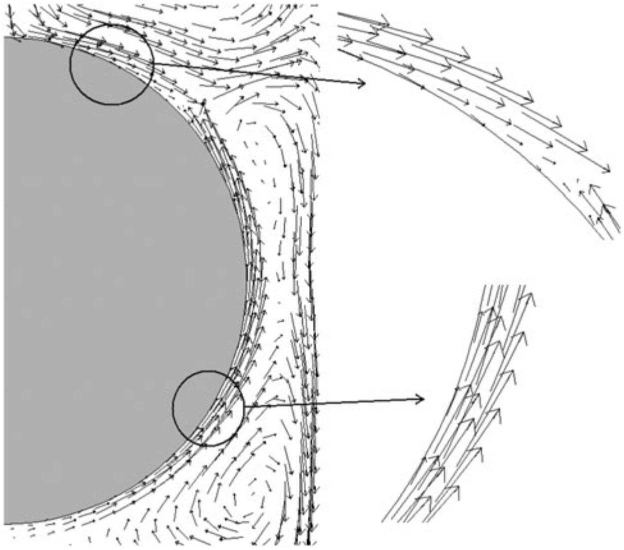

Fig. 4. The fluid velocity vector around the tube at $\Delta T = 9.5$°C and $\dot{m}_f = 0.001\,\mathrm{kg/s}$.

In order to more clarify the main phenomenological aspects of the problem, the vapor volume fraction contour of 0.999 around the tube for the case of $\Delta T = 9.5$°C and $\dot{m}_f = 0.001\,\mathrm{kg/sis}$ drown in Fig. 5. As

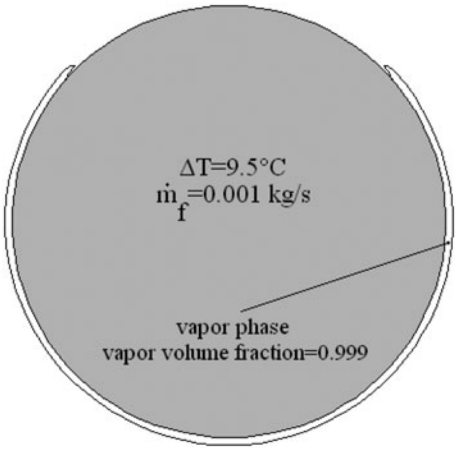

Fig. 5. The vapor volume fraction contour corresponds to 0.999 around the tube at $\Delta T = 9.5$°C and $\dot{m}_f = 0.001\,\mathrm{kg/s}$.

already mentioned, Fig. 5 describes that the major portion of the fluid at the lower part of the tube is vapor. It can also be found that liquid water is dominant at the top of the tube.

To perceive the physical aspects of the problem more clearly, the local heat transfer coefficient around the tube wall is depicted in Fig. 6 at $\Delta T = 9.5^\circ\text{C}$ and $\dot{m}_f = 0.001\,\text{kg/s}$. As mentioned earlier, at the upper side of the tube, the majority of the fluid is liquid water which flows downward with gravitational force. Because of the high thermal conductivity of liquid water, the local heat transfer coefficient is relatively high in this region (high heat transfer coefficient region). At the lower side of the tube, the dominant fluid is water vapor. This water vapor acts like a thermal resistant layer and the heat of the tube should transfer through this layer to the domain fluid. Since the thermal conductivity of water vapor is lower than the thermal conductivity of liquid water, the local heat transfer coefficient at the lower part of the tube wall is not as high as the local heat transfer coefficient at the upper part of the tube.

A comparison is carried out in Fig. 7 to investigate the effect of inlet mass flow rate at different temperature differences on the average heat transfer coefficient. The average heat transfer coefficient is an arithmetic mean defined based on the following formula:

$$\bar{h} = \frac{1}{n}\sum_{i=1}^{n} h_i \tag{34}$$

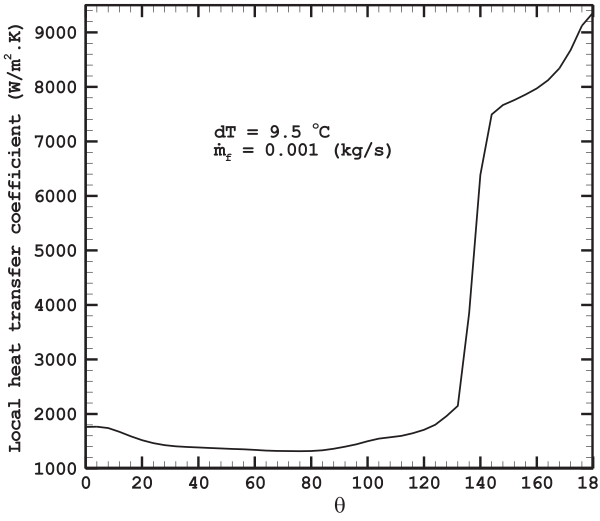

Fig. 6. The local heat transfer coefficient around the tube wall at $\Delta T = 9.5^\circ\text{C}$ and $\dot{m}_f = 0.001\,\text{kg/s}$.

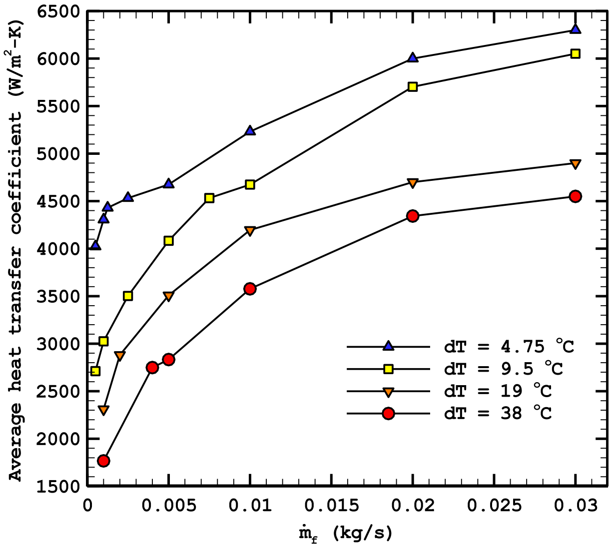

Fig. 7. The average heat transfer coefficient with the inlet mass flow rate at different temperature differences.

where h_i and n are the local heat transfer coefficient and the total number of discrete computational nodes available in the tube surface. The results show, at a constant temperature difference, the average heat transfer coefficient increases by increasing the inlet mass flow rate. For instance, at $\Delta T = 9.5^\circ\text{C}$, while varying the inlet mass flow rate from 0.001 to 0.01 kg/s, the heat transfer coefficient increases 55%. To perceive this increase in average heat transfer coefficient, the vapor volume fraction contour corresponds to 0.99 around the tube at $\Delta T = 9.5^\circ\text{C}$ and two different inlet mass flow rates are depicted in Fig. 8. As can be noticed from this figure, by increasing the inlet mass flow rate at a constant temperature difference, the thickness of the thermal resistant layer declines. So, the average heat transfer coefficient is increased. It is worthwhile to depict the local heat transfer coefficient around the tube wall for the two cases mentioned in Fig. 8. As Fig. 9 shows, increasing the inlet mass flow rate at a constant temperature difference causes the heat transfer coefficient to increase. This increase is for different reasons at the upper and lower sides of the tube. At the upper side of the tube, the fluid velocity and the convective heat transfer effects are raised by increasing the inlet mass flow rate. So, the local heat transfer coefficient is increased. While at the lower part of the tube, the increase in the local heat transfer coefficient is because of decrease in the thickness of a thermal resistant layer.

It can also be found from Fig. 7 that the average heat transfer coefficient declines by increasing the temperature difference at a constant inlet mass flow rate.

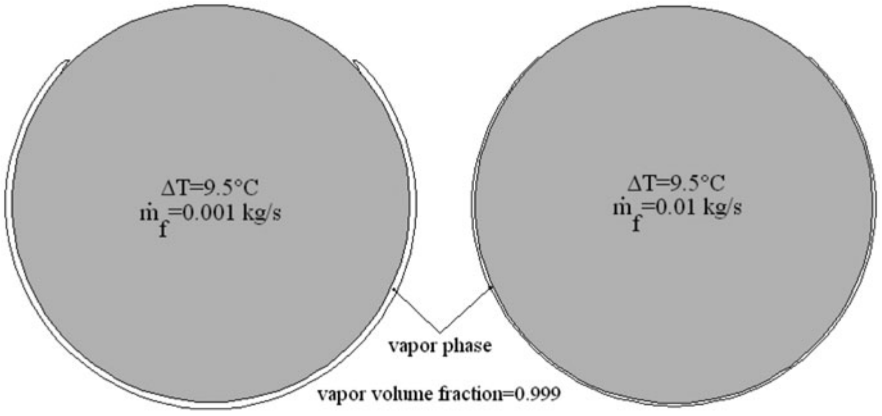

Fig. 8. The vapor volume fraction contour corresponds to 0.99 at $\Delta T = 9.5$°C and two different inlet mass flow rates (0.001 kg/s and 0.01 kg/s).

For example, at $\dot{m}_f = 0.005\,\text{kg/s}$, varying the temperature difference from $\Delta T = 4.75$°C to $\Delta T = 9.5$°C, the heat transfer coefficient decreases 12%. To understand the effect of temperature difference on the flow pattern, the vapor volume fraction contour corresponds to 0.99 around the tube at $\dot{m}_f = 0.005\,\text{kg/s}$ and two distinct temperature differences are depicted in Fig. 10. As this Figure clearly describes, at a constant inlet mass flow rate, increasing the temperature difference is accompanied by increasing the thickness of thermal resistant layer. This means the average heat transfer coefficient around the tube is decreased. To perceive the effect of temperature difference on heat transfer, the local heat transfer coefficient around the tube wall is shown in Fig. 11. When the temperature difference increases from 4.75 to 19°C at a constant inlet mass flow rate, the high heat transfer coefficient region is dramatically shrunk. This is largely due to the stretching of water vapor layer to the top side of the tube. In addition, Fig. 11 shows the local heat transfer coefficient is decreased when the temperature difference increases at a constant inlet mass flow rate.

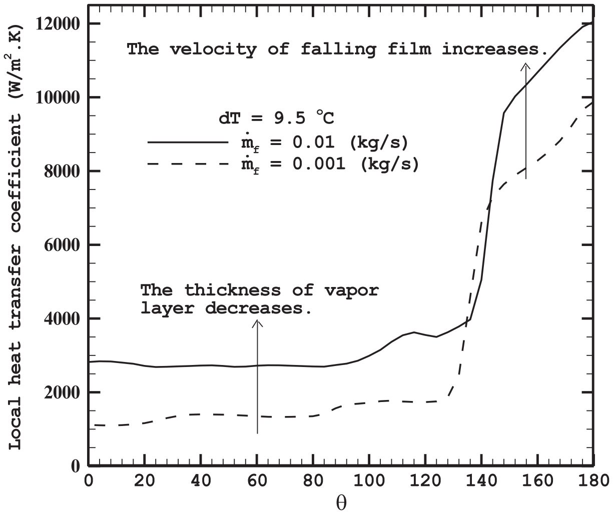

Fig. 9. The local heat transfer coefficient around the tube wall at $\Delta T = 9.5$°C and two different inlet mass flow rates (0.001 kg/s and 0.01 kg/s).

The variation of the net water vapor production vs. the inlet mass flow rate for different temperature differences is shown in Fig. 12. The net water vapor production is closely related to heat flux which has two distinct parameters at a specified geometry, h and ΔT. As observed, at a constant temperature difference between the tube temperature and the saturation temperature, an increase in the inlet mass flow rate causes an increase not only in the heat transfer coefficient but also in the net water vapor production. For instance, the net water vapor production increases 71% by varying the inlet mass flow rate from 0.001 to 0.01 kg/s at $\Delta T = 9.5$°C. On the other hand, as the temperature difference increases at a constant inlet mass flow rate, the net water vapor production which is closely related to the heat flux shifts towards higher values. For example, at $\dot{m}_f = 0.005\,\text{kg/s}$, varying the temperature difference from $\Delta T = 4.75$°C to $\Delta T = 9.5$°C, the net water vapor production rises 54%. To explain this phenomenon, one should pay attention to the heat transfer coefficient and the temperature difference. The results show that the increasing effect of the temperature difference on the net water vapor production is more considerable than the decreasing effect of the heat transfer coefficient. At this point, it is desirable to show the variations of the heat flux ($q'' = h\Delta T$) as a function of

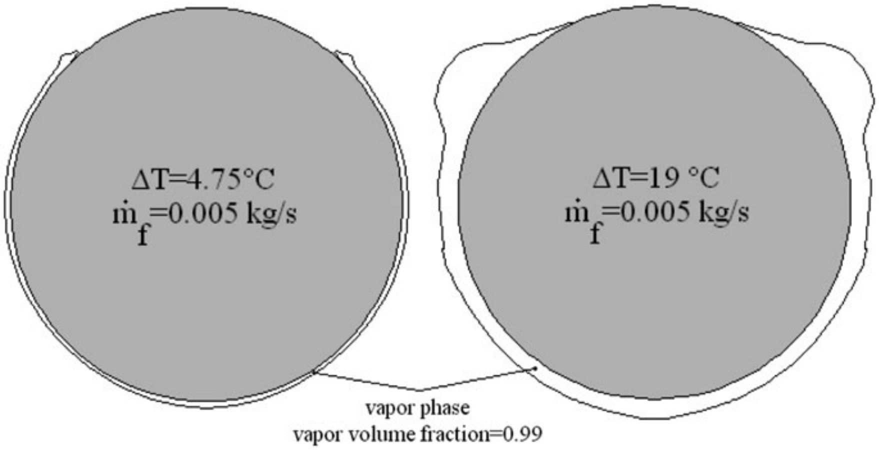

Fig. 10. The vapor volume fraction contour corresponds to 0.99 at $\dot{m}_f = 0.005\,\mathrm{kg/s}$ and two different temperature differences ($\Delta T = 4.75$°C and $\Delta T = 19$°C).

the inlet mass flow rate and the temperature difference. These variations are shown in Fig. 13. At a constant inlet mass flow rate, when the temperature difference increases, the heat flux experiences two different effects, i.e. the declining effect of the heat transfer coefficient and the increasing effect of the temperature difference on the heat flux. As this figure shows, the latter effect is more significant than the former effect on the heat flux. So, the heat flux is increased.

A comparison is carried out in Fig. 14 to investigate the effect of the inlet mass flow rate and the temperature difference on the percentage of net water vapor production (i.e. the ratio of the net water vapor production to the inlet mass flow rate). As shown, when the inlet mass flow rate increases at a constant temperature difference, the percentage of net water vapor production is decreased. In other words, the vapor quality is decreased with increasing the inlet mass flow rate. For instance, the percentage of net water vapor production decreases 83% by varying the inlet mass flow rate from 0.001 to 0.01 kg/s at $\Delta T = 9.5$°C.

One of the prominent applications of falling film evaporation is in multieffect desalination with thermal vapor compression (MED-TVC) plants. MED is a distillation process often used for sea water desalina-

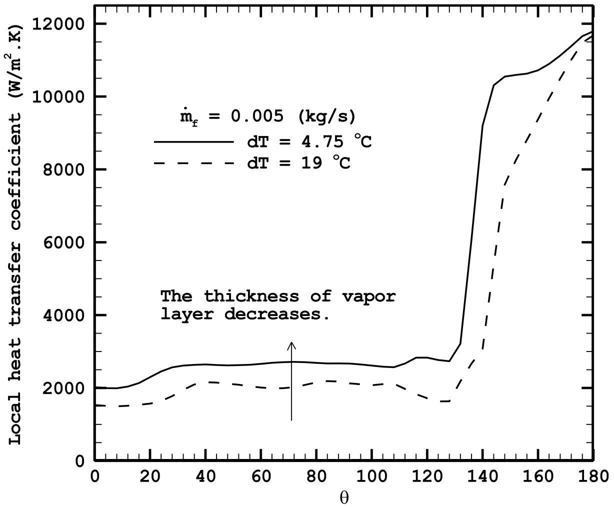

Fig. 11. The local heat transfer coefficient around the tube wall at $\dot{m}_f = 0.005\,\mathrm{kg/s}$ and two different temperature differences ($\Delta T = 4.75$°C and $\Delta T = 19$°C).

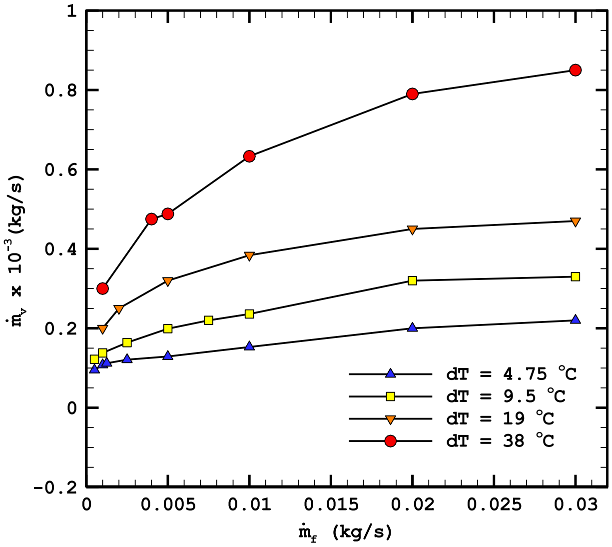

Fig. 12. Variation of the net water vapor production vs. the inlet mass flow rate at different temperature differences.

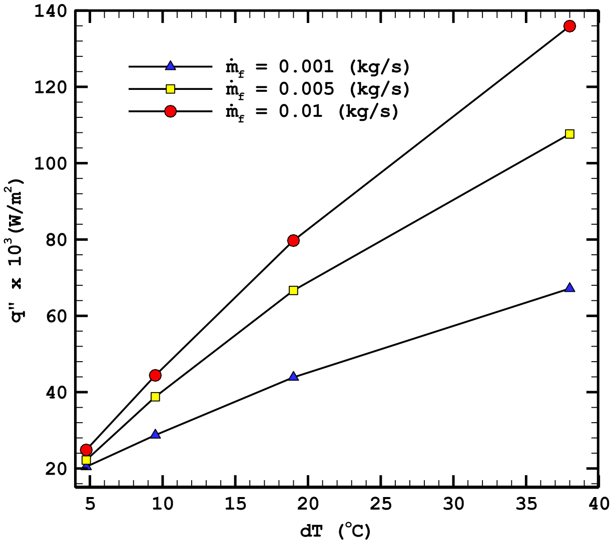

Fig. 13. Variation of the heat flux with temperature differences at different inlet mass flow rates.

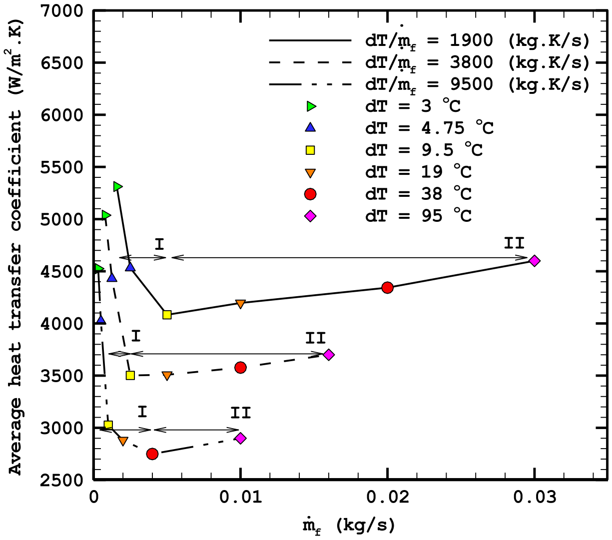

Fig. 15. Variation of the average heat transfer coefficient with the inlet mass flow rate at different $\Delta T/\dot{m}_f$.

tion. It consists of multiple stages or effects. In each effect, the feed water which is sprayed on the top of a horizontal tube bundle is heated by steam in tubes. In the design of MED plants and in order to calculate the number of effects and the required heat transfer area, the basic approach is to assume that the proportion of ΔT to $\dot{m}_f$ is constant. This approach is used in the following results. The variation of the heat transfer coefficient vs. the inlet mass flow rate for different values of $\Delta T/\dot{m}_f$is depicted in Fig. 15. As shown, the diagram has two different trends. In the region I, as the inlet mass flow rate and consequently the temperature difference increases, the heat transfer coefficient is decreased. As already stated, the effects of the temperature difference and the inlet mass flow rate on the heat transfer coefficient are different. This means in Region I, the effect of temperature difference on the heat transfer coefficient is more dominant than the effect of inlet mass flow rate. In contrast, in Region II, the heat transfer coefficient is raised when the value of $\Delta T/\dot{m}_f$increases. In other words, this means that the effect of the inlet mass flow rate on the heat transfer coefficient is more noticeable in Region II.

Fig. 16 shows the variation of the net water vapor production vs. the inlet mass flow rate for different values of $\Delta T/\dot{m}_f$. As can be noticed, the net water vapor production is raised when the inlet mass flow rate increases. At a constant value of $\Delta T/\dot{m}_f$, when the inlet mass flow rate is raised, the temperature difference is also increased. Both of these parameters have an increasing effect on the net water vapor production. For instance, at $\Delta T/\dot{m}_f = 3800$, varying the inlet mass flow rate from 0.00125 kg/s and $\Delta T = 4.75$°C to 0.0025 kg/s and $\Delta T = 9.5$°C, respectively, the net water vapor production increases 46%.

The percentage of net water vapor production, $\dot{m}_v/\dot{m}_f$, at different values of $\Delta T/\dot{m}_f$ is plotted in Fig. 17. As observed, the vapor quality is decreased when the inlet mass flow rate increases at a constant value of $\Delta T/\dot{m}_f$. For instance, the vapor quality

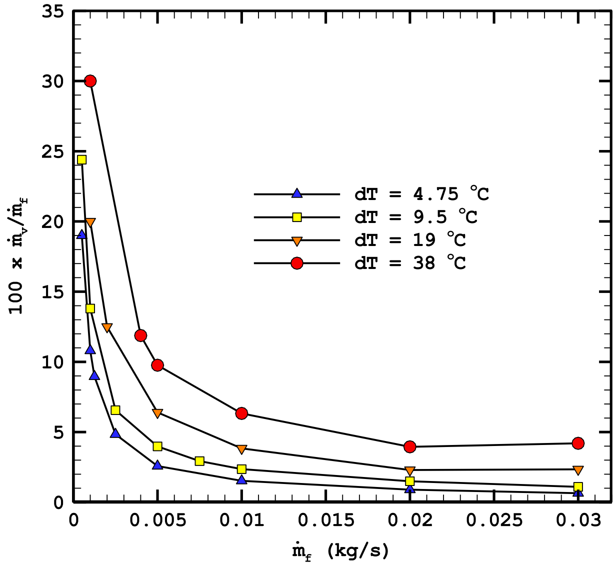

Fig. 14. Variation of the net water vapor production vs. the inlet mass flow rate at different temperature differences.

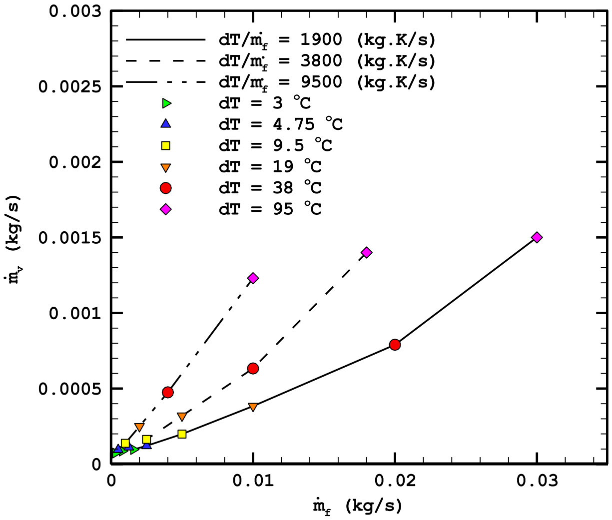

Fig. 16. Variation of the net vapor water production with the inlet mass flow rate at different $\Delta T/\dot{m}_f$.

decreases 49% by variation of the inlet mass flow rate from 0.000316 to 0.004 (kg/s) at $\Delta T/\dot{m}_f = 9{,}500$.

7. Experimental verification

The operational data of two MED-TVC units with a 64 ton/hour capacity are chosen to compare these data with the numerical simulation. The difference between these two systems is that one of them is a MED-TVC unit with four effects while the other is a MED-TVC unit with two effects. Fig. 18 shows a schematic of these MED-TVC units.

A photo of human machine indicator (HMI) of these units is shown in Fig. 19. The desalination units are automatically controlled from the UCP. The industrial data for two MED-TVC units are presented in Table 1 [23].

The average temperature difference between the tube temperature and the effect temperature in each effect of the two experimental units is 4.8 and 10.5°C

Fig. 18(a). A schematic of experimental unit with four effects.

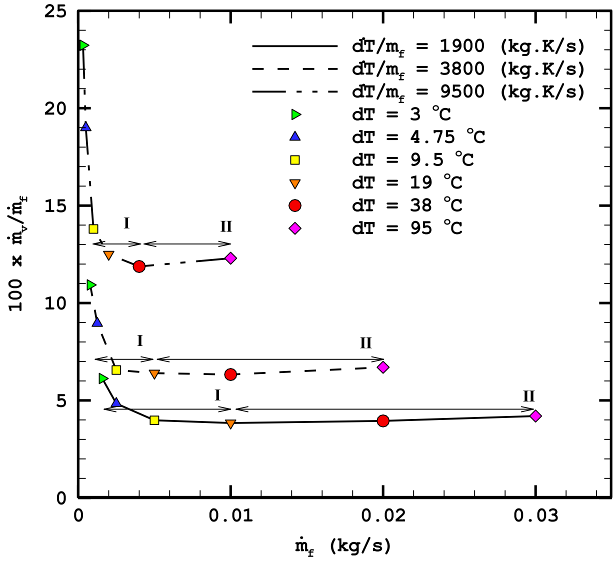

Fig. 17. Variation of the net water vapor production percentage vs. the inlet mass flow rate at different $\Delta T/\dot{m}_f$.

Fig. 18(b). A schematic of experimental unit with two effects.

Fig. 19. A schematic of HMI.

for the MED unit with four and two effects, respectively. The proportion of ΔT to $\dot{m}_f$in both experimental units is approximately 3,600.

Since the total distillated product in two units is the same, it can be concluded as:

$$\left.\frac{\bar{h}_{2\text{ effects}}}{\bar{h}_{4\text{ effects}}}\right|_{\text{Experimental Data}} = \frac{(A\Delta T)_{4\text{ effects}}}{(A\Delta T)_{2\text{ effects}}} = 0.9 \tag{35}$$

This means, at a constant value of $\Delta T/\dot{m}_f$, the average heat transfer coefficient is decreased when the number of effects in the MED desalination units is reduced (or the feed water mass flow rate in each effect is increased). As already discussed, numerical simulations demonstrate that the average heat transfer coefficient may be decreased or increased by increasing the feed water mass flow rate at a constant value of $\Delta T/\dot{m}_f$(Region I or II in Fig. 15). To understand how specific MED desalination unit operates in which region, one should notice the values of $\Delta T/\dot{m}_f$ and the temperature difference. Regarding the given data in Table 1 and calculated data, both mentioned experimental units would work in Region I. At the next step, the numerical code is executed according to the conditions of the two experimental units. For the case of $\Delta T/\dot{m}_f = 3{,}600$ and $\Delta T = 4.8$℃ (corresponding to the MED unit with four effects), the numerical simulation gives 4,410 ($\text{W/m}^2\,\text{K}$) for the average heat transfer coefficient. For the case of $\Delta T/\dot{m}_f = 3{,}600$ and $\Delta T =$ 10.5℃ (corresponding to the MED unit with two effects), the average heat transfer coefficient is 3,654 ($\text{W/m}^2\,\text{K}$). Therefore

$$\left.\frac{\bar{h}_{2\text{ effects}}}{\bar{h}_{4\text{ effects}}}\right|_{\text{Numerical Data}} = 0.83 \tag{36}$$

Table 1
The operational data of two MED-TVC units [23]

Number of effects	4	2
Total distillated product, ton/hr	64	64
Total feed water mass flow rate, ton/hr	216	216
Feed water mass flow rate per effect, ton/hr	54	108
Steam consumption, ton/hr	9.6	21
Entertainment ratio	0.875	0.7
Feed water temperature, ℃	45	45
Discharge temperature, ℃	65	70.7
First effect temperature, ℃	59.8	59.8
Second effect temperature, ℃	55.1	49.7
Third effect temperature, ℃	50.5	–
Forth effect temperature, ℃	45.7	–
Condenser temperature, ℃	45.2	49.2
Specific heat transfer surface area	216	108

As observed, the numerical calculation like the experimental data show that the average heat transfer coefficient declines by decreasing the number of effects in the MED desalination units (or increasing the feed water mass flow rate) at a constant value of $\Delta T/\dot{m}_f$. It can be calculated that the difference between the experimental data extracted from these MED-TVC units and the corresponding numerical data is about 7.7%.

8. Conclusion

Two-phase flow simulation of falling film evaporation phenomenon on a horizontal bundle tube has been studied using the VOF multiphase model based on a PLIC method in curvilinear coordinate. Simultaneous interphase heat and mass transfer during the phase change is also taken into account. The governing equations including continuity, energy, and RANS equations with the k–ε turbulence model are solved by a finite volume method code based on the SIMPLE algorithm and non-orthogonal discretization grid system. Results show that the average heat transfer coefficient increases/decreases by increasing the inlet mass flow rate/the temperature difference at a constant temperature difference/inlet mass flow rate. Results also demonstrate that at a constant value of $\Delta T/\dot{m}_f$ (MED-TVC design approach), as the inlet mass flow rate increases, the heat transfer coefficient may be decreased or increased. This increase or decrease depends on the values of $\Delta T/\dot{m}_f$ and ΔT.

Nomenclature

k — thermal conductivity (W/m K)
h — heat transfer coefficient (W/m^2 K)
k — turbulent kinetic energy (m^2/s^2)
u — velocity component in x-direction (m/s)
y — velocity component in y-direction (m/s)
U — velocity component in ξ-direction (m/s)
V — velocity component in η-direction (m/s)
C_v — heat Capacity (isochoric) (J/kg K)
D_{Sm} — mean Sauter diameter (m)
q_{11} — grid parameter
q_{12} — grid parameter
q_{22} — grid parameter
n — normal direction to the wall
x — horizontal coordinate (m)
y — vertical coordinate (m)
S — source term
h_{lv} — latent heat (J/kg)

Greek symbols

α — volume fraction
ρ — density (kg/m^3)
μ — dynamic viscosity (Pa s)
ξ — curvilinear horizontal coordinate
η — curvilinear vertical coordinate
χ — parameter in equation (19)

Subscripts

l — liquid water
sat — saturation condition
v — vapor
f — feed water

Superscripts

C — contravariant velocities

References

[1] W. Li, X.Y. Wu, Z. Luo, S.C. Yao, J.L. Xu, Heat transfer characteristics of falling film evaporation on horizontal tube arrays, Int. J. Heat Mass Transfer 54 (2011) 1986–1993.

[2] A. Åsblad, T. Berntsson, Surface evaporation of turbulent falling films, Int. J. Heat Mass Transfer 34 (1991) 835–841.

[3] W.H. Parken, Heat transfer to thin films on horizontal tubes, PhD Thesis, Rutgers University, 1975.

[4] Y. Fujita, M. Tsutsui, Experimental investigation of falling film evaporation on horizontal tubes, Heat Trans. Jpn. Res. 27 (1998) 609–618.

[5] J.R. Thome, Falling film evaporation: State-of-the-art review of recent work, J. Enhanc. Heat Trans. 6 (1999) 263–277.

[6] M.C. Chyu, A.E. Bergles, An analytical and experimental study of falling-film evaporation on a horizontal tube, J. Heat Transfer 109 (1987) 983–990.

[7] W.H. Parken, L.S. Fletcher, V. Sernas, J.C. Han, Heat transfer through falling film evaporation and boiling on horizontal tubes, J. Heat Transfer 112 (1990) 744–750.

[8] L. Yang, S. Shen, Experimental study of falling film evaporation heat transfer outside horizontal tubes, Desalination 220 (2008) 654–660.

[9] M. Habert, J.R. Thome, Falling-film evaporation on tube bundle with plain and enhanced tubes—Part i: Experimental results, Exp. Heat Trans. 23 (2010) 259–280.

[10] M. Habert, J.R. Thome, Falling-film evaporation on tube bundle with plain and enhanced tubes—Part ii: New prediction methods, Exp. Heat Trans. 23 (2010) 281–297.

[11] H. Shokouhmand, S. Bigham, Slip-flow and heat transfer of gaseous flows in the entrance of a wavy microchannel, Int. Commun. Heat Mass Transfer 37 (2010) 695–702.

[12] Y.A. Hassan, H.R. Barsamian, New-wall modeling for complex flows using the large eddy simulation technique in curvilinear coordinates, Int. J. Heat Mass Transfer 44 (2001) 4009–4026.

[13] Z. Yang, X.F. Peng, P. Ye, Numerical and experimental investigation of two phase flow during boiling in a coiled tube, Int. J. Heat Mass Transfer 51 (2008) 1003–1016.

[14] G. Son, V.K. Dhir, Numerical simulation of saturated film boiling on a horizontal surface, J. Heat Transfer 119 (1997) 525–533.

[15] M.H. Yuan, Y.H. Yang, T.S. Li, Z.H. Hu, Numerical simulation of film boiling on a sphere with a volume of fluid interface tracking method, Int. J. Heat Mass Transfer 51 (2008) 1646–1657.

[16] S. Zaleski, Interface tracking—VOF, in: Lecture Given at Course: Industrial Two-phase Flow CFD, von Karman Institute for Fluid Dynamics, Belgium, 2005.

[17] J. Li, Piecewise linear interface calculation, Comptes Rendus de Academie des Sciences Serie II. Fascicule B-Mecanique, Technical report, 1995.

[18] W.H. Lee, A pressure iteration scheme for two-phase flow modeling, in: T.N. Veziroglu (Ed.), Multiphase Transport Fundamentals, Reactor Safety, Applications, vol. 1, Hemisphere Publishing, Washington, DC, 1980.

[19] C. Crowe, M. Sommerfeld, Y. Tsuji, Multiphase Flows with Droplets and Particles, CRC Press, New York, NY, 1998.

[20] S.V. Patankar, A calculation procedure for heat, mass and momentum transfer in three dimensional parabolic flows, Int. J. Heat Mass Transfer 15 (1972) 1787–1806.

[21] K.A. Hoffman, Computational Fluid Dynamics for Engineers, Engineering Education System, Austin, 1989.

[22] D.B. Spalding, A novel finite difference formulation for differential expressions involving both first and second derivatives, Int. J. Numer. Methods Eng. 4 (1972) 551–559.

[23] http://www.fanniroogroup.com/.